Mineralogy and Petrology
https://doi.org/10.1007/s00710-024-00878-x

RESEARCH

Lattice strain model for rare earth element partitioning between apatite and silicate melt: effect of apatite/melt composition and temperature with implications for lunar basalts

Markéta Jirků[1] · Václav Špillar[1] · Alessandro Fabbrizio[2]

Received: 15 December 2023 / Accepted: 1 November 2024

Abstract

We present new parameterized lattice strain models to predict the apatite/silicate melt partition coefficients of the rare earth elements (REE) in natural magmatic systems as a function of temperature and melt composition with high accuracy and precision. We collected published experimental REE partition coefficients for apatite coexisting with melt ranging from picrobasaltic to rhyolitic and phonolitic composition. Resulting dataset was analysed using the lattice strain model to assess the data quality. The three lattice strain parameters (D_0, r_0, and E) were subjected to a multivariate nonlinear least-squares analysis as a function of intensive variables, and we attempted to develop two independent models, on the basis of melt and apatite composition. In melt composition-based model, it was found that the D_0 parameter increases with increasing melt polymerization, which can be expressed by the newly proposed simplified melt polymerization index P.I. = $(X_{SiO_2}+2X_{Al_2O_3}+X_{TiO_2}+2X_{P_2O_5})/(X_{MgO}+X_{FeO}+X_{CaO}+2X_{alk})$, where individual X_i variables represent the molar fractions of the oxides in the melt. By disentangling the effect of each component of the P.I., it was found that the CaO content of the melt is the oxide that affects more the D_0 parameter. Thus, the D_0 parameter is expressed as a power law function of melt CaO content. Through extensive search of the parameter space, the E and r_0 variables were found to correlate strongly with linear combination of melt CaO, P_2O_5 and of reciprocal temperature, $1/T$. Based on the apatite composition, we could not find any dependence of the partitioning parameters on compositional variables that would outperform solely a reciprocal temperature-based fit. The new parameterization was applied to predict REE partition coefficients in lunar basalts and suggests that lunar apatite could only equilibrate with evolved melt at late stages of fractional crystallisation.

Keywords Predictive model · REE partition coefficients · Apatite · Fractional crystallisation · Lunar basalts

Introduction

Apatite is a common accessory mineral in igneous, metamorphic, and sedimentary rocks (Webster and Piccoli 2015). It occurs as the most common phosphate mineral and represents a solid solution between fluorapatite (FAp), hydroxylapatite (OHAp), and chlorapatite (ClAp), although in magmatic systems fluorapatite is the dominant member. However, apatite composition is complex and involves multiple substitution schemes.

Apatite lattice is also quite tolerant of vacancies, substitutions, and solid solutions and may host a quantity of distinct ions, e.g., Ca on M1 and M2 sites can be replaced by Mn, Sr, Ba, Pb, Na, Ce, La, Y, Bi, Cd, Co, K or vacancies; PO_4 on $^{IV}XO_4$ site by HPO_4, VO_4, AsO_4, SiO_4 or CO_3, SO_4, BO_4. The site Y is typically occupied by F^-, OH^-, or Cl^- ions, but these can also be substituted by ½CO_3 or ½O (Elliott et al. 2002). Many studies have demonstrated that the M sites in apatite can also be occupied by almost all rare earth elements (REEs) (e.g.Hughes et al. 1991; Fleet and Pan 1995, 1997; Fleet et al. 2000b).

Editorial handling: C. Wang.

✉ Markéta Jirků
jirkuma@natur.cuni.cz

[1] Institute of Petrology and Structural Geology, Faculty of Science, Charles University, Albertov 6, Prague 12800, Czech Republic

[2] Dipartimento di Scienze dell'Ambiente e della Terra - DISAT, Universitá degli Studi di Milano-Bicocca, Piazza dell'Ateneo Nuovo, Milano 1-20126, Italia

Published online: 13 December 2024

Geochemical modelling and partitioning analysis of REE between minerals and coexisting melt provides quantitative evidence concerning igneous differentiation on various scales (Watson and Harrison 1984). Specifically apatite, as a common mineral phase in igneous rocks, plays significant role in the evolution of magmas (Kovalenko et al. 1982; Watson and Harrison 1984). The coefficients of REE partitioning between apatite and melt can be employed as sensitive monitors of the arc magma processes and evolution (e.g., Nathwani et al. 2020), the apatite-iron oxide ore deposits formation (Jonsson et al. 2016), and overall magmatic petrogenesis (Bruand et al. 2017). To choose the appropriate partition coefficients for a particular magmatic problem, it is indispensable to understand how these values behave as a function of intensive parameters (pressure, temperature, and composition), and ionic radii of the elements.

Therefore, the major purpose of this study is to formulate a predictive model for the apatite/melt partition coefficients of REE with high accuracy in natural magmatic systems. Such development has already been accomplished for the most common rock-forming minerals such as pyroxenes (Lee et al. 2007; Yao et al. 2012; Sun and Liang 2012, 2013a, b; Dygert et al. 2014), plagioclase (Sun et al. 2017; Schoneveld and O'Neill 2019), amphibole (Shimizu et al. 2017), garnet (Sun and Liang 2013a), olivine (Lee et al. 2007; Sun and Liang 2013a), and alkali-feldspar (White 2003; White et al. 2003), and some models have also been developed for apatite recently (Li et al. 2023; Ji and Dygert 2024).

Two new partitioning models based on temperature and melt composition were developed in this study. The melt composition model has been subsequently extended with the newly published experimental data of Ji and Dygert (2024), Stepanov et al. (2023), and Tailby et al. (2023). In comparison to previous published studies, these melt composition-based predictive models are particularly useful and can readily benefit the community for application to magmatic geochemical problems. These new models demonstrate the influence of the intensive parameters on the REE partition coefficients. Specifically, the new parameterization is applied to lunar basalts for predicting REE concentrations in the residual melt.

Theoretical background

Lattice strain model

In principle, the mineral/melt partition coefficients for isovalent elements show systematic variations as a function of temperature and ionic radii, as described by the lattice strain model (Blundy and Wood 1994):

$$D_j^{\text{mineral-melt}} = D_0 \exp\left[\frac{-4\pi\, E N_A}{RT}\left(\frac{r_0}{2}(r_0 - r_j)^2 - \frac{1}{3}(r_0 - r_j)^3\right)\right], \quad (1)$$

where D_0 is the mineral/melt "strain-compensated" partition coefficient for an element with the ionic radius (r_0) corresponding to the size of a specific site, and r_j is the ionic radius of the element j. The parameter E is an elastic response of the lattice to strain caused by hosting, in a specific lattice site, ions having radii different from the optimal radius (r_0). The symbol R is the universal gas constant, N_A is the Avogadro's number, and T is the absolute temperature (K).

It was shown for various mineral phases (e.g., pyroxene, garnet, amphibole, and plagioclase) that the D_0, E, and r_0 parameters vary as a function of temperature and mineral or melt composition (Wood and Blundy 1997; Yao et al. 2012; Sun and Liang 2012, 2013a, b; Dygert et al. 2014; Shimizu et al. 2017; Sun et al. 2017). In this study, we explore such kind of dependencies for the apatite/melt partitioning of trivalent elements, namely REE.

Correlation of apatite/melt REE partition coefficients with temperature, pressure and melt composition

The dependence of apatite/melt elemental partition on temperature, pressure, and apatite/melt composition is complex and not fully understood. In previous studies the apatite/melt partition coefficients were determined from natural and experimental samples. These studies have been performed on basaltic, andesitic, basanitic, carbonatitic, and granitic melt composition in experimental studies (Watson and Green 1981; Klemme and Dalpé 2003; Prowatke and Klemme 2006; Li and Hermann 2017a, b; Stepanov et al. 2023; Tailby et al. 2023; Ji and Dygert 2024) and investigated natural samples included for example such as rhyolitic glass (Brophy et al. 2011; Padilla and Gualda 2016), phonolitic melts (Li et al. 2023), and andesitic groundmass (e.g. Fujimaki 1986; for more natural rocks ranging from basanitic to rhyolitic and trachytic compositions see chapter Validation of a new models using natural rock composition). While the effect of melt composition on REE partitioning remains unclear, at least previous study of Watson and Green (1981) described some changes in apatite/melt REE partitioning caused by variations in the melt composition. The SiO_2 content of the melt was identified as the main factor positively influencing the apatite/melt partitioning of the REE. This finding was later confirmed by the results of the experimental research of Prowatke and Klemme (2006), who found that the REE partition coefficients increase by approximately one order of magnitude with increasing the

degree of melt polymerization from basaltic to andesitic melt.

The effect of temperature and apatite composition on apatite/melt partitioning was investigated by Li and Costa (2020) who proposed that the partition coefficients vary not only with *T* but also with apatite F-Cl-OH substitution due to non-ideal mixing of the three apatite end-member anions.

Crystal structure and chemistry of REE in apatite

Apatite is one of the most important minerals controlling REE variations in common igneous rocks (Watson and Green 1981; Harrison and Watson 1984; Hoskin et al. 2000). The REE in apatite substitute for Ca into the two M sites (Mackie and Young 1973; Hughes et al. 1989, 1991; Fleet and Pan 1995), i.e., the M1, a larger, ninefold coordinated (CaO_9) site, and the M2, smaller, sevenfold coordinated site (CaO_6X, where X = F^-, Cl^-, and OH^-). While the effect of crystal composition on apatite/melt REE partitioning has been observed in previous studies, these authors show that crystal chemical mechanisms and major controls on REE site occupancy are complex and not yet entirely constrained by theoretical and experimental studies (Hughes et al. 1991; Fleet and Pan 1995, 1997; Fleet et al. 2000a, b).

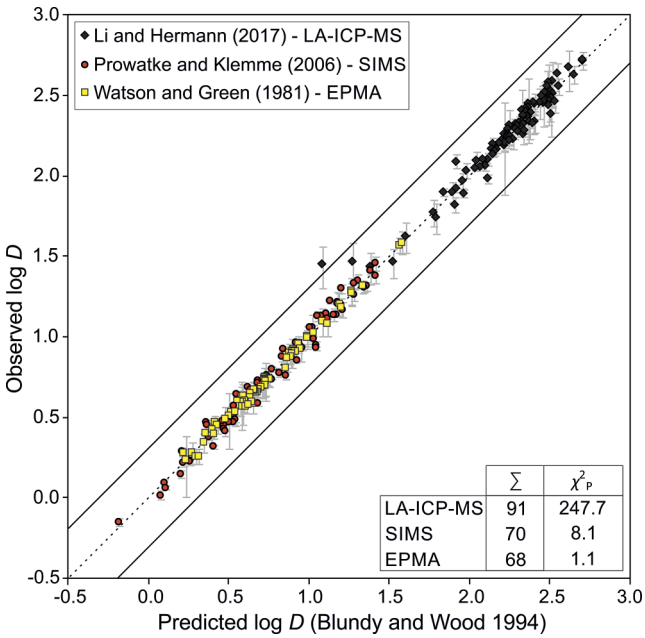

Fig. 1 The data used for the parameterization of the new models re-analysed by using the lattice strain equation of Blundy and Wood (1994). Comparison between predicted and observed partition coefficients, *D*, of REE between apatite and melt. First, the three lattice strain model parameters, D_0, r_0 and *E* are calculated from measured experimental partition coefficients. Predicted partition coefficients are then calculated by substituting these parameters back into the equation of Blundy and Wood (1994). The dotted line represents 1:1 and solid lines represent 1:2 and 2:1 ratio, respectively, and the axes are in a decimal log scale. The error bars are one standard deviation (1σ). The χ^2_P is the Pearson's Chi-square calculated according to the Eq. 12 separately for each type of analysed data (see the section on Parameterization procedures). For the list of data, see Tables 1 and 2. Analytical methods: EPMA – electron probe micro-analysis; LA-ICP-MS – laser ablation-inductively coupled plasma-mass spectrometry; SIMS – secondary-ion mass spectrometry

Previous studies show that the REE can either have preference to enter the M1 site (Urusov and Khudolozhkin 1974), or the M2 site (Borisov and Klevtsova 1963), or that they have no particular preference for these two sites at all (Cockbain and Smith 1967). In detail, Hughes et al. (1991) demonstrated the increasing preference for the M1 site from the lightest (La^{3+} to Pr^{3+}) to mid-light REE (Sm^{3+}). Later, Fleet and Pan (1995, 1997) and Fleet et al. (2000b) noted that the preference of light REE to enter the M2 site depends on the volatile anion content (i.e., F^-, Cl^-, OH^-) in the synthetic apatite. For synthetic ClAp, Fleet et al. (2000a) mention the preference of REE for the M1 site, contrasting to M2 preference in FAp and OHAp. In this case, however, the occupancy of M2 site decreases with increasing atomic number from LREE to HREE. In summary, the REE site preference in apatite is still unclear and difficult to predict.

Methods

Data compilation, criteria, and re-analysis

For the development of the model, we used published REE apatite/melt partitioning data that were re-analysed using the lattice strain model of Blundy and Wood (1994, 2003) to assess the data quality (Fig. 1). In total, we compiled an initial set of experimental partitioning studies from which the calibration dataset was carefully selected following the procedure established by previous workers (Lee et al. 2007; Yao et al. 2012; Sun and Liang 2012, 2013a, b; Dygert et al. 2014; Shimizu et al. 2017; Sun et al. 2017; Schoneveld and O'Neill 2019) to decrease uncertainties in the model calibration. In detail, great care was taken to remove potentially non-equilibrium partitioning data from the calibration dataset, for which the following rejection criteria were applied: (*i*) the experimental products with obvious concentric chemical zoning or heterogeneity between the crystal core and the rim; (*ii*) the experimental products with significant variations from the usual composition of major and trace elements. Moreover, all Eu partition data were removed from our database as these are potentially sensitive to oxygen fugacity, as it has already been shown in several other mineral phases, e.g., pyroxenes (Lee et al. 2007; Fabbrizio et al. 2021), and plagioclase (Aigner-Torres et al. 2007), and we expect similar behaviour also for apatite (Hauri et al. 1994; Blundy et al. 1998; Gaetani et al. 2003; McDade et al. 2003). In addition, experiments reporting less than four

Table 1 Data sources, experimental run conditions and analytical methods

Reference	N^a	N^b	T (K)	P (GPa)	Duration (h)	SiO_2 (wt%)	Na_2O (wt%)	K_2O (wt%)
Melt: LA-ICP-MS; apatite: regression of LA-ICP-MS data								
Li and Hermann (2017)*	9	91	1073	2.5	119–168	62.38–64.91	3.57–5.45	3.24–4.18
SIMS								
Prowatke and Klemme (2006)	10	70	1523	1	4–19.5	41.83–65.18	2.12–17.39	0.68–3.87
EPMA (SEM-equipped)								
Watson and Green (1981)	17	68	1223–1393	0.75–2.0	3–12	41.92–72.88	3.21–4.38	1.12–3.28
Total range			1073–1523	0.75–2.5	3–168	41.83–75.02	41.83–75.02	0.68–4.18

N^a = number of experiments; N^b = number of partitioning data; SEM = scanning electron microscope. The SiO_2, Na_2O, and K_2O in melt are normalised to a total of 100 wt% of all major oxides

Comments: * - while analytically controversial (Ji and Dygert 2024), we prefer to keep the data of Li and Hermann (2017) within the calibration dataset since (*i*) these data cover more felsic (SiO_2 > 60 wt%, MgO < 0.5 wt%) and polymerized (20 < "polymerization index" < 52) part of the melt compositional spectrum by which it considerably extends the range of the model calibration, and (*ii*) inclusion of these data does not compromise the fit quality in the compositional range of other data (lower SiO_2 and melt polymerization)

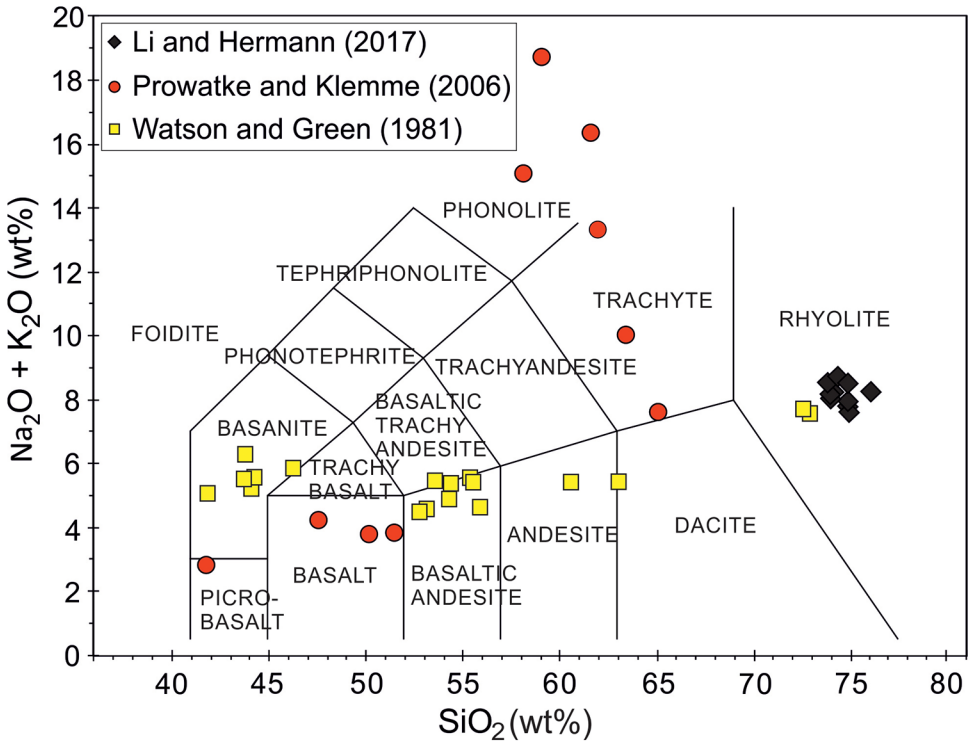

Fig. 2 The TAS diagram showing the synthetic melt compositions used for the calibration of our models. For the list of publications with further details of data sources, see Table 1

REEs were removed due to an insufficient data for a reliable fitting of the lattice strain equation (Eq. 1, see below).

After applying the above criteria, three relevant partitioning studies remained in our calibration dataset of apatite/melt partition coefficients (Table 1), which include a total of 36 apatite/melt partitioning experiments and 237 individual partitioning data. The listed experimental runs had been performed by piston-cylinder apparatus and cover a wide range of melt compositions from picrobasalt to rhyolite and phonolite (SiO_2 content of 41.8 to 75.0 wt%, Na_2O: 2.1 to 17.4 wt%, and K_2O: 0.7 to 4.2 wt%), as illustrated in TAS diagram (Fig. 2). The experiments were performed on a temperature and pressure scale ranging from 1073 to 1523 K and from 0.75 to 2.5 GPa, respectively, and the experimental products were analysed by either laser ablation-inductively coupled plasma-mass spectrometry, LA-ICP-MS (9 experiments with 91 partitioning coefficients; Li and Hermann 2017), secondary-ion mass spectrometry, SIMS (10 experiments with 70 partitioning coefficients; Prowatke and Klemme 2006), and electron probe microanalysis, EPMA (17 experiments with 68 partitioning coefficients; Watson and Green 1981).

For each experiment in the dataset, partition coefficients of multiple REEs (at least four) were available. The lattice strain equation (Eq. 1) has been used to fit the selected sets of apatite/melt partition coefficients, taking their standard deviations into account. The resulting Onuma diagrams yielded lattice strain parabolas (Onuma et al. 1968) showing

variations of the measured partition coefficients as a function of their ionic radius. For each individual experiment, we determined the D_0 (ranging from 3.5 to 178.9 in the whole dataset), E (80–438 GPa), and r_0 (1.0639–1.1607 Å) parameters (Table 2) relevant for a given experimental pressure, temperature, and composition. If not provided in the original source, the overall standard deviations of measured partition coefficients were calculated using the standard deviation for the solid phase composition (subscript "*s*") and that of the coexisting melt composition (subscript "*l*") by the expression:

$$\sqrt{\left(\frac{1}{Average_l}\right)^2 * (SD_s)^2 + \left(\frac{Average_s}{(Average_l)^2}\right)^2 * (SD_l)^2}, \quad (2)$$

where *Average* represents the average concentration of an element in both apatite and melt and *SD* its standard deviations.

Due to the controversial site preference of REE in apatite (see the section The crystal structure and chemistry of REE in apatite and their substitution mechanisms), we have assumed the larger, ninefold coordination on M1 (CaO_9) site. During the calculation of the lattice strain parameters (D_0, r_0, E), the ionic radii of individual REE ions, r_j, were thus taken from Shannon (1976) assuming trivalent charge and ninefold coordination (ranging 1.032–1.216 Å). By this choice, we tried to avoid errors caused by the additional calculations of missing values as Shannon (1976) does not provide the ionic radii for many REEs in sevenfold coordination.

After fitting the apatite/melt partition coefficients, further elimination of data from the calibration dataset was performed according to the goodness of fit (R^2) parameter of the lattice strain parabolas in Onuma diagrams (Onuma et al. 1968). Partition coefficients not fitting well to the parabola ($R^2 < 0.9$) were discarded. After this last elimination, our fitting database included a total of 229 partitioning measurements.

Subsequently, for a purpose of control and data-quality check, the D_0, E, and r_0 parameters were employed to re-calculate the partition coefficients by the Eq. 1. This approach resulted in a good agreement with initially observed values (Fig. 1). Next, the values of the lattice strain model parameters (D_0, E, r_0) served as a starting point for the parameterization procedure described below, in which two separate models were derived relating these parameters to T, P, and composition of melt and of apatite.

Parameterization procedures

To develop a parameterized model for the partitioning of REE between apatite and silicate melt, we used the filtered experimental data that were re-worked using a multivariate nonlinear least-squares analysis. We followed the parameterization procedure of previous studies (Yao et al. 2012; Sun and Liang 2012, 2013a, b; Shimizu et al. 2017; Sun et al. 2017). After the data selection described in the previous section, the obtained D_0, r_0 and E parameters were used to explore their dependence on temperature, pressure, and composition of melt and of apatite, respectively, to assess the variables with greatest influence on the partitioning behaviour.

We assume that the strain-free partition coefficient, D_0, follows the general form of Shimizu et al. (2017):

$$\ln D_0 = a_0 + \frac{a_1}{RT} + f\left(X, \frac{P}{T}\right), \quad (3)$$

where f is a function of apatite/melt composition, X, pressure, P, and temperature, T. The symbol R represents the ideal gas constant, and a_0 and a_1 are the model parameters. Similarly, we treat E and r_0 as functions of P, T, and X, but, for simplicity, we keep the relationships linear and additive for individual contributions:

$$r_0 = b_0 + b_1 T + b_2 P + \sum b_j X_j, \quad (4a)$$

$$E = c_0 + c_1 T + c_2 P + \sum c_j X_j. \quad (4b)$$

In Eqs. 4a and 4b, b_0, b_1, b_2, b_j, c_0, c_1, c_2, and c_j are the model parameters, and the summation index j goes over relevant compositional variables defined as mass percentages, X_j, of apatite or melt, respectively. To distinguish between

Table 2 The range of D_0, r_0, and E parameters and of melt composition (CaO, P_2O_5)

Reference	D_0	r_0 (Å)	E (GPa)	CaO (wt%)	P_2O_5 (wt%)
Melt: LA-ICP-MS; apatite: regression of LA-ICP-MS data					
Li and Hermann (2017)	533.60–178.97	1.0639–1.1594	80.3–399.3	0.73–1.30	0.22–0.44
SIMS					
Prowatke and Klemme (2006)	3.53–28.59	1.1384–1.1607	315.8–437.5	6.30–19.36	1.07–6.97
EPMA (SEM-equipped)					
Watson and Green (1981)	4.65–40.27	1.1126–1.1436	216.3–310.0	2.71–13.06	0.30–3.98
Total range	3.53–178.97	1.0639–1.1607	80.33–437.5	0.73–19.36	0.22–6.97

D_0, r_0, E = determined key partitioning parameters from each experiment (see Eq. 1)

the models based on melt and apatite composition, we use the lower case (the melt model) and the upper case (the apatite model) notation for all model parameters a_i, b_i, c_i (or A_i, B_i, C_i, respectively).

The parameterization procedure we employed is inspired by, but not identical to, the method used in comparable studies on clinopyroxene (Sun and Liang 2012), plagioclase (Sun et al. 2017), or amphibole (Shimizu et al. 2017). In contrast to these works, we first perform stepwise linear least square analysis to find the main factors affecting D_0 and create its final fit according to the Eq. 3. The E and r_0 parameters appear jointly in the exponential of the lattice strain equation (Eq. 1; Blundy and Wood 1994). Therefore, these variables are intercorrelated and not completely independent (Sun and Liang 2012). To account for this, we fit the whole exponential of the Eq. 1 using the expressions for E and r_0 (Eq. 4) inserted into the Eq. 1. This approach allows us to overcome the need of fitting the whole dataset simultaneously to highly non-linear formulation and helps to solve the convergence issues. Also, fitting D_0 separately from E and r_0 avoids introducing artificial correlations, which can occur in simultaneous fitting of all three parameters.

By exploring the parameter space of the Eq. 3 for melt, we found that D_0 is best expressed as a non-linear power law function of CaO content of melt, $X_{\mathrm{CaO}}^{\mathrm{melt}}$ (wt%; for CaO correlation, see the Discussion section, see also Appendix A – Fig. S1 for correlations with other compositional variables). Interestingly, the single-parameter correlation of $\ln D_0$ with CaO is even stronger then with SiO_2, as observed previously (Watson and Green 1981; see the Discussion section). The fit performance may be marginally improved by adding linear dependencies on the reciprocal temperature, $1/T$, and TiO_2 content of melt. However, we consider such improvement insufficient to balance the addition of two fit parameters and we prefer to keep the formulation in a simple power law form:

$$\ln D_0^{\mathrm{melt}} = a_2 \left(X_{\mathrm{CaO}}^{\mathrm{melt}}\right)^{a_3}, \tag{5}$$

where a_2 and a_3 are the fit coefficients contained in the function f of the Eq. 3, and a superscript "melt" indicates melt composition-based fit. Note that the parameters a_0 and a_1 of the Eq. 3 are not employed in the final fit (Eq. 5).

For the apatite fit, despite an extensive search, we could not find satisfactory dependence of D_0 on any compositional variable. This is understandable due to rather limited range of the solid solution between the three end-members of apatite. Within our dataset, even the most abundant and the most variable components, CaO and P_2O_5, do not vary more than ~15% of their content. Therefore, we resigned to create a composition-based fit and only keep A_0 and A_1 parameters of the Eq. 3 to account for the temperature dependence of partitioning:

$$\ln D_0^{\mathrm{Ap}} = A_0 + \frac{A_1}{RT}. \tag{6}$$

Through an extensive search of the compositional variables and their combinations, we found that both E and r_0 parameters of the melt model correlate strongly with CaO and P_2O_5. Leaving any of these two variables significantly worsened the fit, whereas addition of some other compositional parameter did not lead to significant improvement. Also, both E and r_0 appeared to be temperature dependent, but relatively insensitive to pressure variations. Therefore, we modelled both parameters in the following forms:

$$r_0^{\mathrm{melt}} = b_0 + b_1 T + b_3 X_{\mathrm{P_2O_5}}^{\mathrm{melt}} + b_4 X_{\mathrm{CaO}}^{\mathrm{melt}}, \tag{7a}$$

$$E^{\mathrm{melt}} = c_0 + c_1 T + c_3 X_{\mathrm{P_2O_5}}^{\mathrm{melt}} + c_4 X_{\mathrm{CaO}}^{\mathrm{melt}}, \tag{7b}$$

where the b_2 and c_2 coefficients related to the pressure terms were omitted (cf. Equation 4).

For the apatite model, the search of the compositional space led to analogous formulations based on phosphorus and calcium content. Due to the very same reason as for the D_0 model, the X_{CaO} and $X_{\mathrm{P_2O_5}}$ terms might be omitted without significant adverse effect on the fit performance (~3% increase of standard residual error). For simplicity, we thus modelled the E and r_0 parameters as functions of T only:

$$r_0^{\mathrm{Ap}} = B_0 + B_1 T, \tag{8a}$$

$$E^{\mathrm{Ap}} = C_0 + C_1 T. \tag{8b}$$

Technically, in the least-square fitting of the D_0 parameter, we minimize the chi-square of the logarithmic values, which is beneficial when dealing with quantities ranging multiple orders of magnitude:

$$\chi^2 = \sum_{j=1}^{N} \left(\ln D_{0,j} - \ln D_{0,j}^{\mathrm{m}}\right)^2. \tag{9}$$

In the last equation, the superscript "m" denotes the coefficient extracted by the re-analysis of measured dataset (the section on Data compilation, criteria, and re-analysis), whereas absence of the superscript indicates the value predicted by our fit (Eqs. 5 and 6, respectively), and subscript j sums over all D_0 data (N=36). For E and r_0 values, we minimize the chi-square:

$$\chi^2 = \sum_{j=1}^{M} \left(\epsilon_j - \epsilon_j^{\mathrm{m}}\right)^2, \tag{10}$$

where ε stands for the whole exponential term in the Eq. 1, i.e.:

$$\epsilon_j = \frac{-4\pi E N_{\mathrm{A}}}{RT}\left(\frac{r_0}{2}(r_0 - r_j)^2 - \frac{1}{3}(r_0 - r_j)^3\right), \tag{11}$$

where N_{A} is the Avogadro's constant, and where the indices follow the same notation as in the Eq. 9, but the subscript j now sums over all partitioning data measurements ($M = 229$) and the site radius, r_j, relates to the element relevant to that specific measurement. The predicted ε values were calculated using our model Eq. 7 or 8, respectively, for E and r_0 parameters. In both fitting procedures, the R environment and its "stats" package was employed (R Core Team 2021).

To assess the overall fit performance, we report the Pearson's chi-square values of the partition coefficients defined as

$$\chi^2_{\mathrm{P}} = \sum_{j=1}^{M} \frac{\left(D_j - D_j^{\mathrm{m}}\right)^2}{D_j}. \tag{12}$$

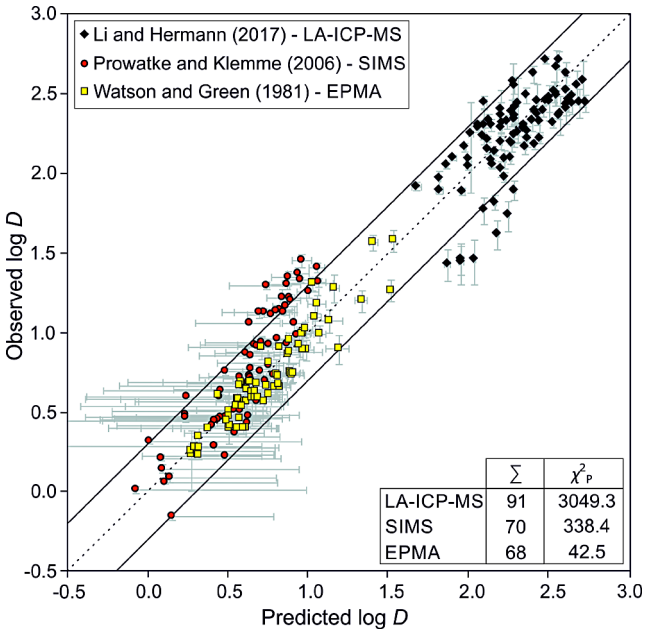

Fig. 3 The comparison of predicted and observed partition coefficients, D, of REE between apatite and melt based on the melt composition (Eq. 13a–c). The dotted line represents 1:1 and solid lines represent 1:2 and 2:1 ratio, respectively, and the axes are in a decimal log scale. The error bars of the observed and predicted values are one standard deviations (1σ). The χ^2_{P} is the Pearson's Chi-square calculated according to the Eq. 12 separately for each type of analysed data (see the section on Parameterization procedures). For the list of data, see Table 2. Abbreviations as in Fig. 1

In the last equation, D_j^{m} is measured partition coefficient from the measurement j, D_j is its predicted value, and the index j sums over all partitioning measurements ($M = 229$). All data used to develop the models are available in Table S1 as Supplementary material.

Results

Mathematical findings

Based on 36 apatite/melt partitioning experiments covering a wide range of pressure (from 0.75 to 2.5 GPa) and temperature (from 1073 to 1523 K; Table 1) and 229 individual partitioning data contained in our filtered dataset, we propose the following expressions relating the parameters of the lattice strain equation (Eq. 1, Blundy and Wood 1994) to silicate melt composition and temperature (Fig. 3; see chapter Discussion and Appendix A – Fig. S1 for correlation graphs):

$$\ln D_0^{\mathrm{melt}} = 5.16\,(\pm 0.11) \times \left(X_{\mathrm{CaO}}^{\mathrm{melt}}\right)^{-0.416(\pm 0.018)}, \tag{13a}$$

$$r_0^{\mathrm{melt}} = 7.191\,(\pm 2.041) \times 10^{-5} T + 3.723\,(\pm 2.388) \times 10^{-3} X_{\mathrm{P_2O_5}}^{\mathrm{melt}} - 15.600\,(\pm 8.123) \times 10^{-4} X_{\mathrm{CaO}}^{\mathrm{melt}} + 1.047\,(\pm 0.022), \tag{13b}$$

$$E^{\mathrm{melt}} = 0.366\,(\pm 0.157) \times T + 6.112\,(\pm 17.580) \times X_{\mathrm{P_2O_5}}^{\mathrm{melt}} - 7.388\,(\pm 6.004) \times X_{\mathrm{CaO}}^{\mathrm{melt}} - 135.8\,(\pm 168.7), \tag{13c}$$

where $X_{\mathrm{CaO}}^{\mathrm{melt}}$ and $X_{\mathrm{P_2O_5}}^{\mathrm{melt}}$ are calcium and phosphorous content of melt (wt%), T is the absolute temperature (K), and units of r_0 and E are angstroms and GPa, respectively. The values in brackets are 1σ error estimates obtained directly by the fitting procedure.

Due to the limited compositional variability of apatite, we could not find satisfactory relationships for D_0, r_0, and E that would complement Eq. 13a–c, based on the apatite composition. Therefore, we propose solely temperature-based model (Fig. 4) in which addition of compositional terms do not lead to significant performance improvements. In case when the melt composition is unknown, we thus suggest using the following formulations taking only temperature into account:

$$\ln D_0^{\mathrm{Ap}} = \frac{12461(\pm 1509)}{RT} - 6.63\,(\pm 1.19), \tag{14a}$$

$$r_0^{\mathrm{Ap}} = 51.91\,(\pm 9.27) \times 10^{-6}\, T + 107.40\,(\pm 1.18) \times 10^{-2}, \tag{14b}$$

$$E^{\mathrm{Ap}} = 0.285\,(\pm 0.068) \times T - 62.7\,(\pm 83.1), \tag{14c}$$

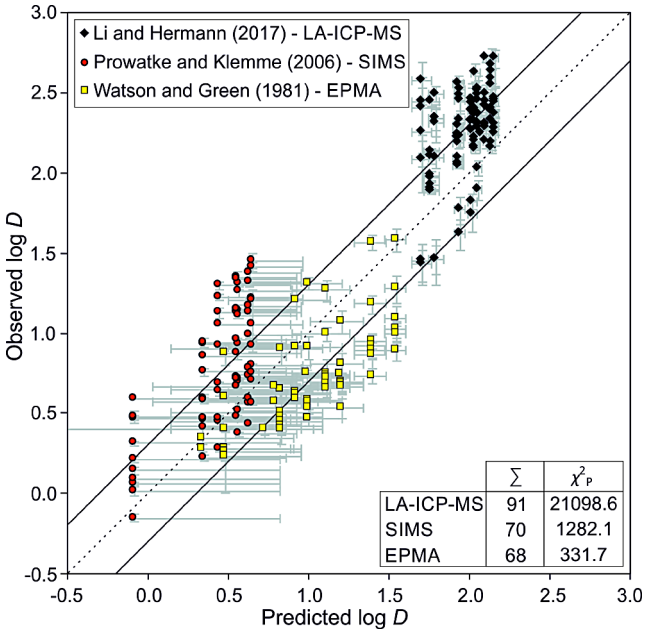

Fig. 4 The comparison of predicted and observed partition coefficients, *D*, of REE between apatite and melt employing the temperature-based model (Eq. 14a–c). The dotted line represents 1:1 and solid lines represent 1:2 and 2:1 ratio, respectively, and the axes are in a decimal log scale. The error bars of observed and predicted values are one standard deviations (1σ). The χ^2_P is the Pearson's Chi-square calculated according to the Eq. 12 separately for each type of analysed data (see the section on Parameterization procedures). For the list of data, see Table 2. Abbreviations as in Fig. 1

where *T* is the absolute temperature (K), *R* the ideal gas constant ($Jmol^{-1}K^{-1}$), units of r_0 and *E* are angstroms and GPa, respectively, and values in brackets are 1σ error estimates from the fitting procedure.

The final model and its comparison between the predicted and the observed partition coefficients of REE based on melt composition is shown in Fig. 3. The Pearson's Chi-square (χ^2_P) is calculated according to Eq. 12, where our melt model generates the χ^2_P values of 3049.3 ($N=91$), 338.4 ($N=70$), and 42.5 ($N=68$) for the data analysed by LA-ICP-MS, SIMS, and EPMA, respectively. Overall, 88% of the predicted partition coefficients (out of a total of 229) fall between 50% and 200% of the measured values (i.e. between 1:2 and 2:1 lines in the Fig. 3). Final model of the REE partitioning based on the temperature is shown in Fig. 4. In this case, the model generates the χ^2_P values of 21098.6 ($N=91$), 1282.1 ($N=70$), and 331.7 ($N=68$) for the data analysed by LA-ICP-MS, SIMS, and EPMA, respectively, which indicates a lower quality compared to the model based on melt composition. For this model, 52% of the predicted partition coefficients (out of a total of 229) fall between 50% and 200% of the measured values (Fig. 4).

For comparison, the Pearson's Chi-square (χ^2_P) was calculated also for the original measured data selected for modelling (Fig. 1). In this case, the obtained χ^2_P values were 247.7, 8.1, and 1.1 for the data analysed by LA-ICP-MS ($N=91$), SIMS ($N=70$), and EPMA ($N=68$), respectively.

The 1σ errors for individual predicted partition coefficients of both models were calculated by ordinary error propagation rules. Some limitations, however, need to be considered regarding the errors of these models. In case of the model based on melt composition, the r_0 and *E* coefficients are correlated to a large extent, which leads to the error overestimation using ordinary error propagation, as the method inherently assumes that the parameters are uncorrelated. The covariance of both coefficients, which would be needed to avoid this issue, is, unfortunately, unavailable. The average 1σ error of the partition coefficients predicted by the melt model is 0.69 of a natural log unit. In the fit of the temperature-based model, the estimated error is greater, 1.74 of natural log unit on average.

Validation of new models using natural rock composition

Data selection

In this section, we test whether the proposed distribution coefficient parameterizations (Eq. 13a–c, 14a–c) are applicable to new data, not used in the original model calibration. For this purpose, published data on apatite and melt composition in natural rocks are employed.

As an independent test of our model parameterization, we derived apparent partition coefficients from the apatite and melt composition pairs from a wide range of natural rock compositions obtained from published literature (in total, 11 articles; Table 3). The database for the check of validity contains 15 samples of natural rocks ranging from basanitic to rhyolitic and trachytic compositions (Fig. 5), with magmatic temperatures from ~1050 to ~1360 K (Table 3). This database provides 226 individual apatite/melt partitioning data of REE.

In case of the temperature-based model (Eq. 14a–c), the predicted partition coefficients for all 226 measurements of individual REE apatite/melt partitioning data contained in the validation database have been calculated. The database for the temperature-based model includes the data analysed by EPMA (1 sample; 9 partitioning coefficients), SIMS (1; 24), LA-ICP-MS (4; 120), isotope dilution mass spectrometer, (ID-MS; 5; 36), SEM (1; 12), sensitive high-resolution ion microprobe (SHRIMP; 1; 11), and by the instrumental neutron activation analysis (INAA; 2; 14).

In case of the model based on melt composition (Eq. 13a–c), it was only possible to calculate 159 predicted partition coefficients as some melt composition values required by the model (CaO or P_2O_5 content) were missing in the

Table 3 Data sources for validation of the models based on natural composition

Reference	N	T (K)	Observed D	r_j (Å)	SiO_2 (wt%)	Na_2O (wt%)	K_2O (wt%)	CaO (wt%)	P_2O_5 (wt%)
EPMA									
Fujimaki (1986)	1	1143[(1)]	13.8–46	1.032–1.216	66.9	3.82	2.47	3.00	0.20
SIMS									
Brophy et al. (2011)	1	1203[(2)]	22.2–80.1	1.075–1.216	72.3	4.41	4.83	0.84	n.a.
LA-ICP-MS									
Arzamastsev et al. (2009)	2	1331–1362[(3)]	0.78–8.04	1.032–1.216	41.0–43.8	1.00–3.28	2.90–3.02	14.53–16.35	0.72–1.31
LA-ICP-(HR)MS (high resolution LA-ICP-MS)									
Fedele et al. (2015)	1	1233[(4)]	7.8–39	1.032–1.216	61.2	6.22	6.87	1.83	n.a.
SEM									
Padilla and Gualda (2016)	1	1053[(5)]	42–253	1.032–1.216	n.a.	n.a.	n.a.	n.a.	n.a.
ID-MS									
Nagasawa (1970)	4	1073[(6)]	11.2–89.8	1.032–1.196	71.3–77.8	3.06–3.80	2.54–3.56	1.18–2.81	0.05–0.09
ID-MS									
Nagasawa and Schnetzler (1971)	1	1173[(6)]	7.9–21.7	1.032–1.196	76.9	3.40	3.66	1.61	0.01
SHRIMP									
Sano et al. (2002)	1	1073[(6)]	33–93	1.032–1.216	n.a.	n.a.	n.a.	n.a.	n.a.
Apatite: EPMA; glass: INAA									
Mahood and Stimac (1990)	1	1223[(7)]	7.2–38	1.032–1.216	63.7	6.42	4.91	1.26	0.07
INAA									
Wörrier et al. (1983)	1	1173[(8)]	24.3–102	1.095–1.196	n.a.	n.a.	n.a.	n.a.	n.a.
LA-ICP-MS									
Li et al. (2023)	1	1223[(9)]	5–30	1.032–1.216	55.8	9.15	5.52	1.95	0.27
Total range		1053–1362	0.79–253	1.032–1.216	41.0–77.8	1.00–9.15	2.47–6.87	0.84–16.35	0.01–1.31

N = number of samples; T = temperature; Observed D = partition coefficients obtained from published literature; r_j = effective ionic radii with ninefold coordination (Shannon 1976); n.a. = not analysed. The SiO_2, Na_2O, K_2O, CaO, and P_2O_5 are melt components normalised to a total of 100% of all major oxides

References: (1) Fujimaki 1986; (2) Brophy et al. 2011; (3) calculated based on SiO_2 content using model of Harrison and Watson 1984; (4) Pelullo et al. 2022 (average); (5) Padilla and Gualda 2016; (6) Venezky and Rutherford 1999; (7) White et al. 2009; (8) Harms et al. 2004; (9) Li et al. 2023

published literature. This validation dataset consists of the data analysed by LA-ICP-MS (3 samples, 105 partitioning coefficients), by EPMA (1, 9), by ID-MS (5, 36), and by INAA (1, 9).

Validation procedure

Compositions and temperatures (Fig. 5; Table 3) of all natural samples chosen for the validation procedure were substituted into the Eq. 13a–c and 14a–c to obtain the lattice strain model parameters (D_0, r_0 and E). These values were then employed to determine the predicted partition coefficients for each individual apatite/melt compositional pair by using the Eq. 1. In all calculations, we expect ninefold coordination of REE in the apatite (e.g., White and Dong 2003; Dong and White 2004a, b; Mercier et al. 2005) and use the effective ionic radii (r_j) reported by Shannon (1976), which ranges from 1.032 to 1.216 Å. The error of the predicted partition coefficients was determined based on ordinary error propagation rules, while for the measured partition coefficient we employed the error provided in the original data source. Where not reported, the error was estimated using the Eq. 2.

Validation results

For both models tested (Eq. 13a–c, 14a–c), we have found predicted values of the REE partition coefficients to agree with the observed validation data (Figs. 6 and 7). Specifically, the melt composition-based fit yields the Pearson's Chi-square values (χ^2_P, Eq. 12) are 627.0 (N = 105), 43.4 (N = 9), 566.0 (N = 36), and 305.4 (N = 9) for the data analysed by LA-ICP-MS, EPMA, ID-MS, and INAA, respectively. Scatter of the predicted vs. observed data around 1:1 line is similar to that of the original fitting dataset (Fig. 6 vs. Figure 3) with 58% of the validation datapoints (out of a total of 159) falling between the 1:2 and 2:1 lines.

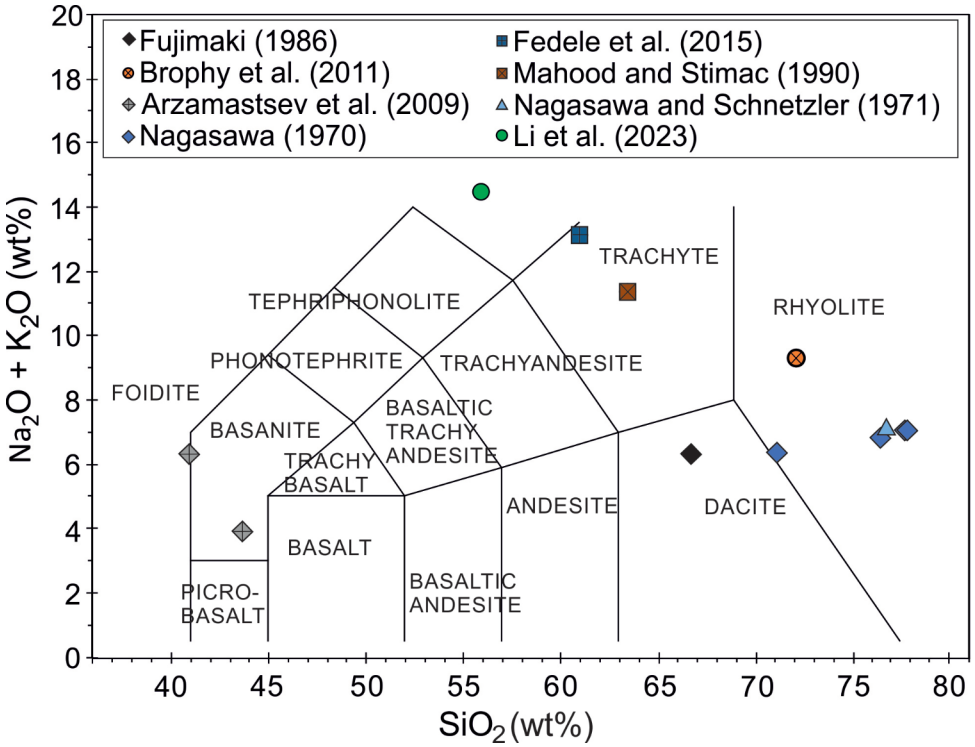

Fig. 5 The TAS diagram showing compositions of natural rocks used to verify the functionality of a new model. Data from Padilla and Gualda (2016), Sano et al. (2002) and Wörrier et al. (1983) could not be plotted due to missing values (SiO_2, K_2O, or Na_2O content). For the list of publications with further details of data sources, see Table 3

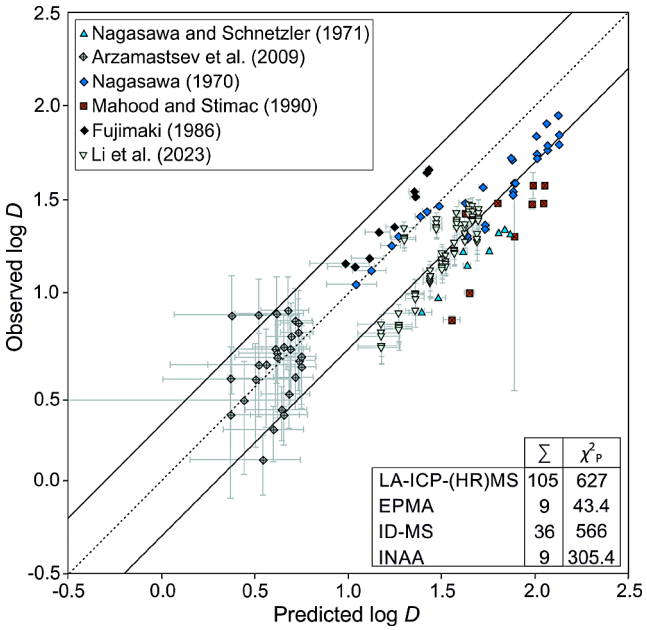

Fig. 6 Verification of the melt composition-based model. The comparison of predicted and observed partition coefficients, *D*, of REE between apatite and melt for the verification dataset based on the melt composition (Eq. 13a–c). The dotted line represents 1:1 and solid lines represent 1:2 and 2:1 ratio, respectively, and the axes are in a decimal log scale. The error bars of observed and predicted values are one standard deviations (1σ). The χ^2_P is the Pearson's Chi-square calculated according to the Eq. 12 separately for each type of analysed data (see the section on Parameterization procedures). For the list of data, see Table 3

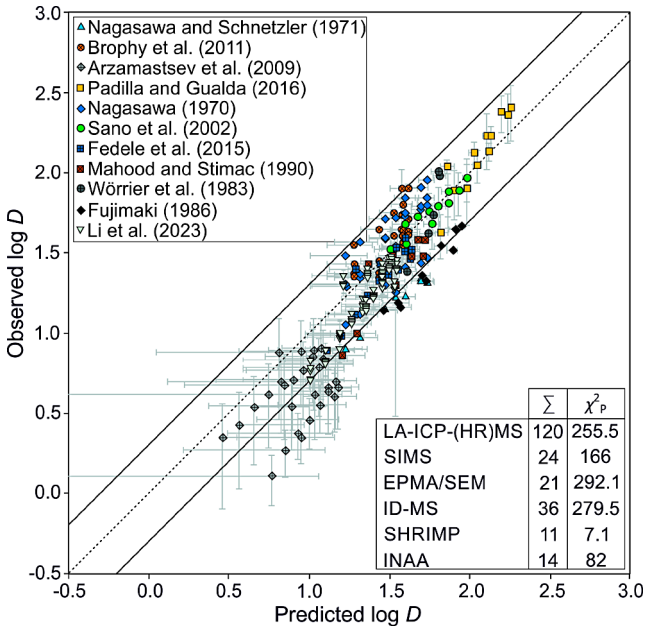

Fig. 7 Verification of the temperature-based model. The comparison of predicted and observed partition coefficients, *D*, of REE between apatite and melt for the verification dataset based on the temperature (Eq. 14a–c). The dotted line represents 1:1 and solid lines represent 1:2 and 2:1 ratio, respectively, and the axes are in a decimal log scale. The error bars of observed and predicted values are one standard deviations (1σ). The χ^2_P is the Pearson's Chi-square calculated according to the Eq. 12 separately for each type of analysed data (see the section on Parameterization procedures). For the list of data, see Table 3

Comparison between the predicted and observed partition coefficients of the REE yielded by the temperature-based model is shown in the Fig. 7. In this case, the χ^2_P values are 255.5 ($N=120$), 166.0 ($N=24$), 292.1 ($N=21$), 279.5 ($N=36$), 7.1 ($N=11$), and 82.0 ($N=14$) for the data analysed by LA-ICP-MS, SIMS, EPMA/SEM, ID-MS, SHRIMP, and INAA, respectively. Scatter of the validation datapoints is visually reduced compared to the fitting dataset (Figs. 7 vs. 4) with almost 89% of the validation datapoints (out of a total of 226) falling between 1:2 and 2:1 lines.

To conclude, the validation procedure has shown that both proposed partitioning models are applicable and perform well when applied to novel data not employed in their original calibration.

Discussion

Role of melt composition on REE partitioning in apatite

Based on the partitioning data contained in our filtered dataset (Table 2), we proposed the expressions relating the lattice strain equation parameters (Blundy and Wood 1994) to the temperature and silicate melt composition (Eq. 13a–c, 14a–c). In principle, elemental partitioning between mineral and melt is dependent on chemistry of both crystal (e.g., Blundy and Wood 1994, 2003) and melt (e.g., Watson 1976; Ryerson and Hess 1978; O'Neill and Eggins 2002).

In our dataset, the melt CaO correlates inversely with the $\ln D_0$ parameter (Fig. 8a; $R^2=0.72$) and proves to be the single most robust factor driving the overall values of the partition coefficients of REE (Eq. 13a, $R^2=0.94$ with power-law relationship). Since the correlation with the melt CaO content exploits the majority of the partitioning data variability, addition of other compositional variables (e.g., Na_2O) does not lead to significant improvement of the fit performance. Alternatively, similar but weaker negative correlations of $\ln D_0$ were observed with the melt TiO_2 ($R^2=0.77$), FeO ($R^2=0.70$), P_2O_5 ($R^2=0.43$), and MgO ($R^2=0.39$) content. In contrast, SiO_2 content itself correlates positively with $\ln D_0$ (Fig. 8b; $R^2=0.63$), as expected by previous authors (Watson and Green 1981; Prowatke and Klemme 2006), but the quality of correlation is lower than with the CaO. However, the same kind of dependence is observed also for the K_2O ($R^2=0.63$), and Na_2O ($R^2=0.41$, considering the data with $Na_2O<5$ wt% only). See Appendix A – Fig. S1 for diagrams of $\ln D_0$ correlations with compositional parameters.

Role of melt structure on REE partitioning in apatite

For the cations with high charge density, a positive correlation between the mineral/melt partitioning coefficient and the degree of melt polymerization was proposed by Ryerson and Hess (1978). The experimental data of Watson and Green (1981) and Prowatke and Klemme (2006) confirmed this effect by finding REE partition coefficient to increase with increasing SiO_2 content.

Interestingly, strong correlations of $\ln D_0$ are observed even with relatively minor melt constituents as is the TiO_2 (ranging 0.15 to 2.22 wt% in our calibration dataset). Moreover, the SiO_2, a major network former, correlates positively with the partition coefficient value, but so do the alkalis as network modifiers, while other tetrahedrally coordinated cations, as Ti or P, behave oppositely. The melt components, however, are not completely independent variables and we suggest that such virtually paradoxical behaviour reflects inter-correlations of individual compositional parameters in the calibration dataset. Due to the negative correlation of the melt SiO_2 content with those of CaO, MgO, FeO, TiO_2, and

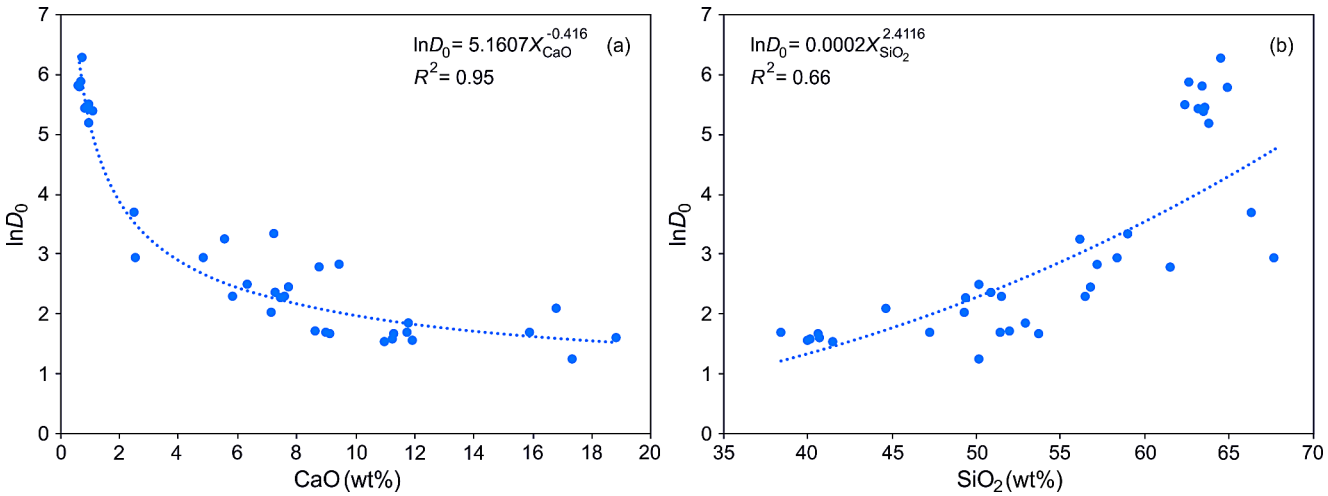

Fig. 8 **a** The inverse correlation of the melt CaO content with the $\ln D_0$ parameter. **b** The positive correlation of melt SiO_2 content with $\ln D_0$ for the experimental data of Li and Hermann (2017), Prowatke and Klemme (2006), and Watson and Green (1981)

P_2O_5 and positive correlation with alkali contents, the $\ln D_0$ value still reflects the overall trend from more primitive to more evolved thus more polymerized melts. To document this behaviour, we constructed a simplified melt polymerization index, P.I., as a molar ratio of supposed network formers to supposed network modifiers:

$$\mathrm{P.I.} = \frac{X_{\mathrm{SiO_2}} + 2 \times X_{\mathrm{Al_2O_3}} + X_{\mathrm{TiO_2}} + 2 \times X_{\mathrm{P_2O_5}}}{X_{\mathrm{MgO}} + X_{\mathrm{FeO}} + X_{\mathrm{CaO}} + 2 \times X_{\mathrm{alk}}}, \quad (15)$$

where individual X_i variables represent molar fractions of oxides in melt. The X_{alk} are alkalis in excess to those needed to charge compensate for Al^{3+} in tetrahedral sites evaluated as $X_{\mathrm{Na_2O}} + X_{\mathrm{K_2O}} - X_{\mathrm{Al_2O_3}}$ in peraluminous melts and considered as zero otherwise. Such P.I. correlates nicely with the $\ln D_0$ (Fig. 9, $R^2 = 0.95$) as it reflects the role of changing melt structure (e.g., Watson and Green 1981; Prowatke and Klemme 2006). The power-law fit of this relationship ($R^2 = 0.95$):

$$\ln D_0 = 1.2055 \times \mathrm{P.I.}^{0.4113}, \quad (16)$$

may substitute our Eq. 13a and may serve on itself as a basis of the predictive partitioning model. Since the Eq. 15, compared to our CaO-based Eq. 13a, brings negligible improvement in predicting $\ln D_0$ values ($R^2 = 0.95$ vs. 0.94 for the fit of the calibration dataset), we preferred to use the calcium-based model in our study due to its simplicity and robustness. On the other hand, since the Eq. 15 is apparently more general in its principle, it might be beneficial when extrapolating to exotic compositions far from these used in the original calibration.

In summary, the proposed P.I., correlating the compositional variables serves as a proxy for the overall melt polymerization and may be employed as a basis of the partitioning parameterization. In our model (Eq. 13a), we opted to use the CaO content due to quality of the resulting power-law fit and large range of its variations (0.6 to 18.8 wt% in the calibration dataset). Relatively speaking, while CaO content ranges more than an order of magnitude, the content of SiO_2 only ranges 38.4 to 68.8 wt%, that is, less than twice of its lower value.

Apart from that, apatite is a Ca-bearing phase thus the activity of calcium drives its stability. The role of melt Ca content on partitioning between the melt and apatite was reported for Ba and Sr (Prowatke and Klemme 2006) and S (Parat and Holtz 2005), but not for REE. Possible role of the "stoichiometric control" (*sensu* O'Neill and Eggins 2002) may represent a direct effect of Ca melt content, other than that related to the melt polymerization, on REE partitioning between apatite and melt.

Role of apatite composition on REE partitioning

Based on the apatite composition, there seems to be not enough variability and systematic correlations to construct robust composition-based fit for the partition coefficients. Within the dataset, even content of the most abundant substituent, SiO_2, only reaches < 2 wt% and it displays no systematic correlation with REE partition coefficient, expressed as $\ln D_0$.

There is a hint of positive correlation between $\ln D_0$ and amount of Al in the apatite ($R^2 = 0.73$). However, due to limited variations of this component (< 0.24 wt% Al_2O_3), it seems improbable that it could reflect any true physicochemical behaviour. Rather, we expect that this correlation is an inherited result of apatite/melt Al partitioning and indirectly reflects compositional variations of the melt. Alternatively, there is some trend between the Cl content and $\ln D_0$ ($R^2 = 0.47$). While some systematic variations of

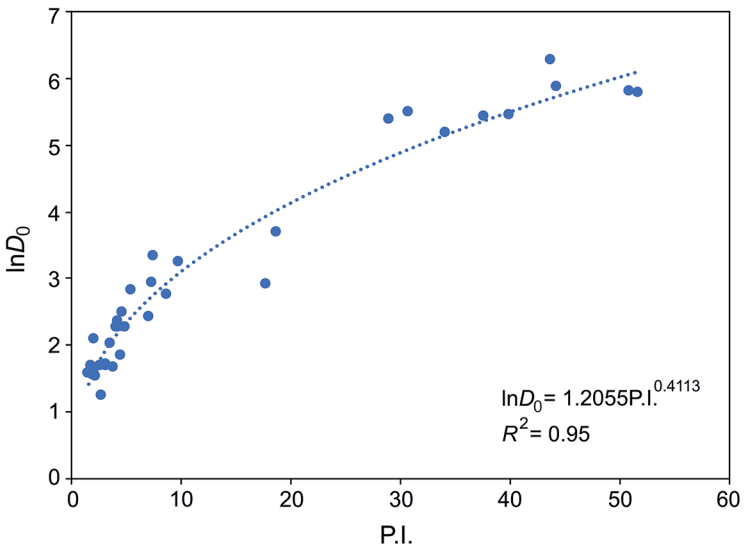

Fig. 9 Correlation of the simplified melt polymerization index (P.I.) with the $\ln D_0$ reflecting the effect of changing melt structure on apatite/melt partitioning for the experimental data of Li and Hermann (2017), Prowatke and Klemme (2006), and Watson and Green (1981)

REE partitioning might be expected as a function of proportions of apatite end-member constituents (Li and Hermann 2017; McCubbin and Ustunisik 2018), the lack of volatile content data for apatite in our dataset precludes any further investigation.

After finalization of our models, some new experimental studies were published. For example, the article of Ji and Dygert (2024) showed the importance of the anion component on REE partitioning. Authors report the results suggesting that REE partitioning is sensitive to anionic site occupancies. In detail, they found out that ClAp exhibits lower REE partition coefficients in comparison with FlAp and OHAp. Since it affects their REE partition coefficients in apatite, it has a direct impact on controlling the substitution mechanisms of REE in apatite structure. Therefore, we decided to incorporate these new data for F^- and OH-bearing systems together with other studies (Stepanov et al. 2023; Tailby et al. 2023; Ji and Dygert 2024) into our dataset to create an additional predictive model, in comparison with Eq. 13.

Implementation of newly published data into the calibration dataset

In this section, we discuss the effect of the new experimental data on apatite/melt REE partitioning, which were published after finalization of the original model (Eq. 13). The new data include studies of Ji and Dygert (2024), Stepanov et al. (2023), and Tailby et al. (2023); a total of 31 partitioning experiments and 272 individual partitioning data for melts (for TAS diagram, see Appendix B – Fig. S2, see also Table S2 as Supplementary material for extended partitioning data), from which it was possible to calculate 201 predicted partition coefficients. This data addition almost doubles the size of the original calibration dataset while most of the novel data fall into the "low D" region ($D<1$). The data treatment followed the same path as described in the "Data compilation, criteria, and re-analysis" section and after re-analysis, the values of $\ln D_0$, E, and r_0 were unified with the original dataset to form a basis for the least-square fitting of the compositional dependencies.

Importantly, after thorough search for the $\ln D_0$ correlations with compositional variables, we arrived at similar conclusions as with the original (smaller) dataset. While $\ln D_0$ correlation with melt SiO_2 content is better than in the original dataset ($R^2=0.77$ vs. 0.66 for power-law fit), the CaO-based fit is still superior ($R^2=0.82$ vs. 0.94 for power-law fit; Fig. 10a) and represents the best available correlation with single compositional variable (see Appendix C – Fig. S3).

In the extended dataset, there is still strong correlation between the $\ln D_0$ and the melt "polymerization index", P.I., calculated according to the Eq. 15, which supersedes the correlation quality of any single compositional variables. With the best-fitting log-log linear functional form this fit yields:

$$\ln D_0 = 1.4763\ (\pm 0.0556) \times \ln \mathrm{P.I.} + 0.0153\ (\pm 0.1003), \quad (17a)$$

with $R^2=0.92$ (Fig. 10b) and where values in brackets are 1σ error estimates from the fitting procedure. Obviously, the interpolation ability of the P.I.-based fit remains unimpaired even after almost doubling the size of the calibration dataset. In this case, however, the log-log formulation is preferred over the power-law fit employed with the original dataset (Eq. 16) since it allows for steeper dependence of $\ln D_0$ on P.I. at the lower range of the P.I. values, where majority of data additions occurred.

For the E and r_0 variables (Eq. 1) in the extended dataset, we again arrived at the same form of the expressions as with the original dataset and both parameters are best expressed as a linear function of temperature and melt CaO and P_2O_5 content:

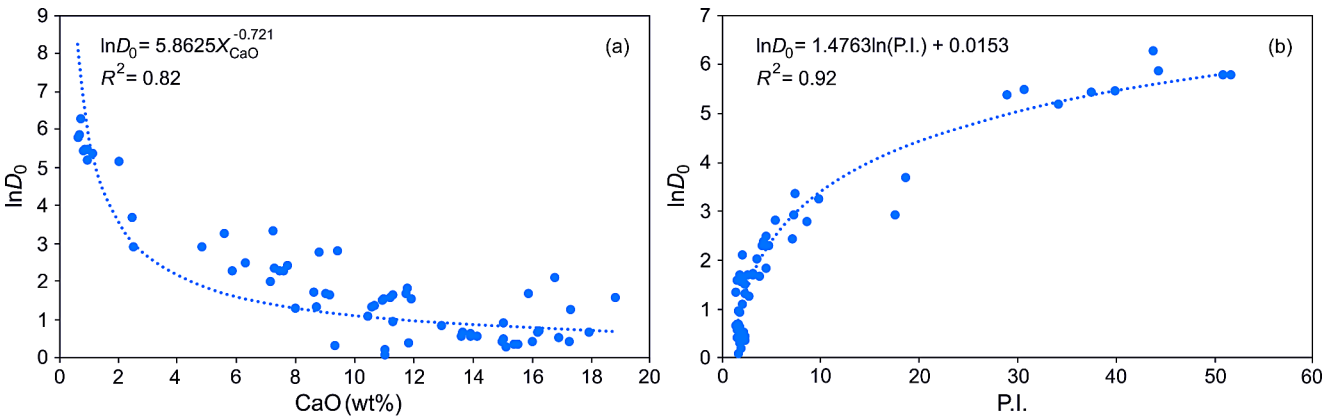

Fig. 10 **a** The correlation of the melt CaO content with the $\ln D_0$ parameter and **b** the correlation of the simplified melt polymerization index (P.I.) with the $\ln D_0$ for the experimental data of Ji and Dygert (2024), Stepanov et al. (2023), and Tailby et al. (2023)

$$r_0^{melt} = 7.654\,(\pm1.168) \times 10^{-5} T + 3.118\,(\pm0.943) \times 10^{-3} X_{P_2O_5}^{melt} - 1.940\,(\pm0.425) \times 10^{-3} X_{CaO}^{melt} + 1.044\,(\pm0.013)\,, \quad (17b)$$

$$E^{melt} = 0.459\,(\pm0.083) \times T + 1.320\,(\pm5.967) \times X_{P_2O_5}^{melt} - 10.04\,(\pm28.77) \times X_{CaO}^{melt} - 261.6\,(\pm91.99)\,, \quad (17c)$$

where X_{CaO}^{melt} and $X_{P_2O_5}^{melt}$ are calcium and phosphorous content of melt (wt%), T is the absolute temperature (K), and units of r_0 and E are angstroms and GPa, respectively. The values in brackets are 1σ error estimates obtained directly by the fitting procedure.

The Eq. 17a–c represent a calibration of the melt composition-based model utilizing novel experimental data of Ji and Dygert (2024), Stepanov et al. (2023), and Tailby et al. (2023) and complement the previous calibration based on the polymerization index (Eq. 13b, c, and Eq. 16). This model and its comparison between the predicted and the observed partition coefficients of REE based is shown in Fig. 11. The Pearson's Chi-square (χ^2_P) is calculated according to Eq. 12, where extended melt model calibration generates the

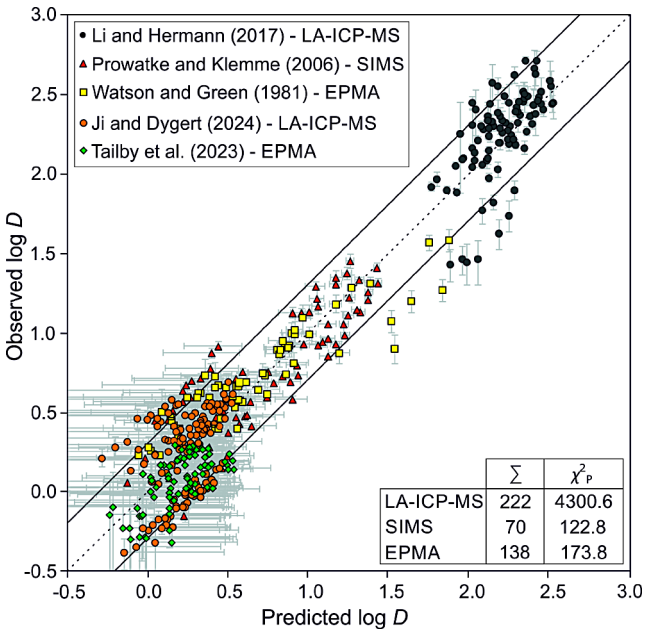

Fig. 11 The comparison of predicted and observed partition coefficients, D, of REE between apatite and melt based on the melt composition for the studies of Li and Hermann (2017), Prowatke and Klemme (2006), Watson and Green (1981) based on Eqns, 13a–c and for the studies of Ji and Dygert (2024), Tailby et al. (2023) based on Eq. 17a–c. The dotted line represents 1:1 and solid lines represent 1:2 and 2:1 ratio, respectively, and the axes are in a decimal log scale. The error bars of the observed and predicted values are one standard deviations (1σ). The χ^2_P is the Pearson's Chi-square calculated according to the Eq. 12 separately for each type of analysed data (see the section on Parameterization procedures). Abbreviations as in Fig. 1

χ^2_P values of 4300.6 (N=222), 122.8 (N=70), and 173.8 (N=138) for the data analysed by LA-ICP-MS, SIMS, and EPMA, respectively. Overall, 83% of the predicted partition coefficients (out of a total of 430) fall between 50% and 200% of the measured values (i.e. between 1:2 and 2:1 lines in the Fig. 11).

After the addition of these new data, no significant changes were observed for the predictive model. In summary, the model calibration utilizing the extended dataset provides performance which is similar to the previous calibration without novel data. It demonstrates that the formulation based on the polymerization index and melt CaO and P_2O_5 content offers robust ground for apatite/melt REE partition coefficient prediction.

Collated experimental dataset with predicted values for the temperature-based model, melt composition-based model, and for the melt composition-based model extended with new data of Ji and Dygert (2024), Stepanov et al. (2023), and Tailby et al. (2023) is available in Table S3–S5 as Supplementary material.

Model application: partition coefficients for lunar magmatism

Melt REE content in equilibrium with lunar apatite

Lunar basalts show the importance of apatite REE content and partition during fractional crystallisation (Boyce et al. 2014; Rapp and Draper 2018). Therefore, we apply our new lattice strain parameterizations to compare how the REE content of residual melt obtained from the published literature corresponds to the composition calculated using distribution coefficients resulting from the new models.

Lunar meteorites provide valuable information on the formation and evolution of the Moon and lunar magmatism (e.g., Shearer and Papike 1999; Hiesinger et al. 2000, 2003; Stadermann et al. 2018). For exemplary application of our new apatite/melt partitioning parameterization, we have chosen to predict the REE content of lunar basaltic melt in equilibrium with apatite based on the lunar apatite composition. While apatite is quite common in lunar basalts, most of the published studies do not provide a full range of REE needed to calculate the equilibrium melt REE concentrations using our model. For this reason, we have chosen the analyses of a lunar meteoritic sample, NWA 10597, provided by Wu and Hsu (2020) as a basis for our modelling (Table 4).

The NWA (Northwest Africa) 10597 is unbrecciated mare basalt found in 2015. This sample is a medium-grained low-Ti mare basalt with a subophitic texture relatively enriched in REE (Wu and Hsu 2020). From the available REE concentrations of apatite in this sample (in total, 3

Table 4 The REE content of bulk melt and of apatite (ppm) in lunar basalt used for the fractional crystallisation model (Wu and Hsu 2020)

Element	Bulk		Apatite	
N	5	Average	3	Average
La	13.3–16.8	15.4	802–1743	1261
Ce	35.2–45.6	41.4	2368–4767	3468
Pr	5.2–6.2	5.8	349–669	499
Nd	27.8–31.0	29.3	1895–3291	2515
Sm	9.5–10.7	10.0	569–984	753
Eu	1.3–1.6	1.4	31–45	37
Gd	11.0–12.4	11.8	680–1175	896
Tb	2.0–2.1	2.0	106–185	140
Dy	13.4–14.2	13.9	622–1113	837
Ho	3.0–3.2	3.1	120–210	160
Er	8.3–9.1	8.6	279–524	386
Tm	1.0–1.1	1.1	32–63	45
Yb	8.0–9.7	8.6	174–347	249
Lu	1.0–1.2	1.1	20–41	29

N = number of average analyses

Table 5 Predicted partition coefficients, $D^{average}$, and predicted melt composition (ppm) in equilibrium with lunar apatite

Element	Predicted $D^{average}$		Predicted $melt^{average}$	
N	3		3	
T (°C)	1177	965	1177	965
La	3.98	14.46	317.1	87.18
Ce	5.36	20.42	647.3	169.81
Pr	6.34	25.19	78.7	19.81
Nd	6.93	28.67	363.1	87.71
Sm	6.84	30.75	110.2	24.49
Eu	6.38	29.69	5.9	1.26
Gd	5.70	27.53	157.1	32.55
Tb	4.96	24.81	28.2	5.64
Dy	4.18	21.66	200.2	38.65
Ho	3.47	18.60	46.1	8.60
Er	2.87	15.85	134.5	24.36
Tm	2.32	13.22	19.5	3.42
Yb	1.84	10.80	135.5	23.05
Lu	1.43	8.66	20.5	3.37

N = number of average analyses

analyses of the apatite by LA-ICP-MS), the equilibrium melt composition was predicted using our temperature-based model (Eq. 14a–c, Table 5) and compared with the bulk rock REE content (in total, 5 analyses of bulk rock composition analysed by LA-ICP-MS) reported by Wu and Hsu (2020) (Table 4). In the modelling, the average values of apatite and bulk rock compositions were employed. The temperature range between two limiting values of 965 and 1177 °C was considered for calculating the REE content in melt. This range represents the estimated liquidus temperature based on the average composition of the fusion crust, and an average temperature based on the coexisting ilmenite and Ti-rich spinel (Wu and Hsu 2020).

The calculated REE content of melt in equilibrium with apatite is overall high and it exceeds chondritic concentrations by a factor of hundreds to more than thousand. As a function of temperature, the calculated equilibrium values are 5 to 30 times higher than in the observed bulk rock composition (Table 4), and the higher temperature implies higher REE content. However, the bulk rock composition is characterized by generally flat-lying REE plot with negative slope gently rising towards slight LREE enrichment, and this trend is well-reproduced also by the calculated equilibrium melt data (Fig. 12).

Calculated REE profile of melt (Fig. 12) exhibits distinct negative Eu anomaly ($Eu/Eu^* = 0.14$ regardless of temperature), which is significantly more pronounced than in the bulk rock composition ($Eu/Eu^* = 0.38$). Although we excluded Eu from the model calibration due to sensitivity of its valence state to redox conditions, the model formulation interpolates the Eu partitioning providing it is fully in trivalent state, in line with other REE. Discrepancy of the observed and calculated Eu anomaly may thus reflect the role of a divalent state expected to dominate in more reducing conditions.

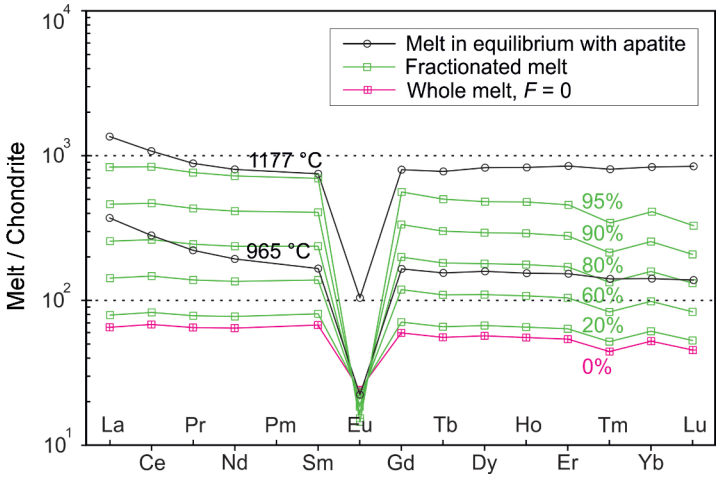

Fig. 12 The REE plot with comparison of predicted lunar basaltic liquid composition in equilibrium with fluorapatite (for temperatures of 965 and 1177 °C; using model Eq. 14a–c combined with Eq. 18) and composition of lunar basaltic melt fractionates at various crystallinity levels, *F*. The *F* = 0 represents original bulk rock lunar basaltic composition before fractional crystallisation. Both melt and apatite compositions and fractionating mineral assembly (61.66% pyroxene, 30.56% plagioclase, 3.30% olivine, 4.37% fayalite, and 0.11% apatite) are based on a lunar basaltic meteorite, NWA 10597 (Wu and Hsu 2020). For Eu, the partition coefficient predicted by the model (Eq. 14a–c) represents value interpolated according to Eu^{3+} ionic radius and providing fully trivalent state. Normalisation to chondritic concentrations according to Anders and Grevesse (1989) was employed

Fractionation of lunar basaltic melts and apatite saturation

Further, we have considered variations of melt REE content during fractional crystallisation which is expected to have played a significant role in crystallisation of the NWA 10597 sample and of lunar basalts in general (Chen et al. 2019; Jiang et al. 2023). In detail, we employed bulk rock and mineral chemistry data to calculate lunar-relevant REE partition coefficients for the most abundant minerals in the studied sample (i.e. pyroxene, plagioclase, olivine, fayalite, and apatite; Wu and Hsu 2020). These partition coefficients were then combined according to the modal composition of the sample to provide bulk distribution coefficients of REE, D_{bulk}, for the crystallising assembly (for details, see Fig. 12 caption). Subsequently, concentrations of individual elements in a differentiated melt, C_L, were evaluated using the fractional crystallisation expression:

$$C_L = C_0 \times F^{(D_{bulk}-1)}, \quad (18)$$

where C_0 is a concentration of a given element in the parental melt and F is a degree of fractional crystallisation. In this approach, components are gradually depleted from melt in the same proportions under which they are present in a fully solidified samples with its actual modal content of solid phases.

In Fig. 12, REE plots resulting from the fractional crystallisation with variable degree, F, are shown along with the melt composition in equilibrium with apatite. As F increases, so does the content of individual REE and for $F > 90\%$ it approaches the expected equilibrium distribution corresponding to the lower limit of considered range of temperatures. The best fit with the equilibrium REE content at expected temperature range is reached for differentiated melt at advanced stages of fractional crystallisation when $F \approx 93$–95%, that is, when ~7–5% of trapped melt remains within the system. The model of fractional crystallisation thus predicts late fluorapatite saturation after reaching ~95% solidification, which is consistent with previous results (Anand et al. 2014).

In detail, the REE pattern predicted by the fractionation model differs slightly in shape compared to the expected equilibrium melt. After 95% of crystallisation, the slope of the mid-heavy to heavy REE segment of fractionated melt is predicted steeper, while the lightest REE segment (La - Pr) appears flatter than expected in the melt in equilibrium with apatite (Fig. 12). While these effects may reflect an inherent behaviour of the partitioning parameterization, it may as well represent an artifact of simplifications involved in the fractionation model; specifically, assumed simultaneous crystallisation of all phases according to their modal proportions.

In summary, the newly proposed parameterization of REE partitioning between apatite and melt allows to predict realistic REE patterns for lunar basaltic melts based on the apatite composition. It implies late saturation of apatite after reaching ~97% of crystallisation followed by equilibration of apatite with a small amount of REE-enriched trapped melt.

Conclusions

In this study, we present new parameterized lattice strain models for the REE partitioning between silicate melt and apatite. Over a wide range of P-T-X_{melt}, we propose expressions relating partitioning parameters, D_0, E, and r_0, of the lattice strain model temperature and melt calcium and phosphorous content. The strain-free partition coefficient, D_0, increases with increasing degree of melt polymerization expressed as a function of the proposed P.I. ratio. Since compositional parameters of melt are generally correlated along usual fractionation trends, multiple components, including SiO_2 or CaO, may be employed as a single main factor driving the D_0 value. In this work, we opted to develop CaO-based formulation due to best fit quality compared to choices based on other compositional parameters. However, it remains unknown if melt CaO content plays any other role in determining the D_0 value beyond contributing to the overall melt depolymerization. Due to limited compositional variability of apatite, we failed to develop complementary formulation for partition coefficient based on the apatite composition. Instead, solely temperature-based model is proposed, since addition of compositional terms does not lead to significant improvement of the fit performance.

The new parameterizations reported in this study represent significant improvement in predicting apatite/melt partitioning of REE needed to understand REE budget during igneous fractionation. When tested against published partitioning data derived from natural igneous rocks, both melt composition and temperature-based formulations are found to provide satisfactory agreement with observed data. Application of the temperature-based model to the composition of lunar basalts points to relatively high REE contents (La 87 to 317 ppm at $T = 965$ and 1177 °C, respectively; Lu 3 to 20 ppm at $T = 965$ to 1177 °C, respectively) in melt equilibrating with the apatite. This finding is consistent with late apatite saturation in lunar basaltic magmas and implies that it equilibrated with $< 5\%$ of residual liquid.

Supplementary Information The online version contains supplementary material available at https://doi.org/10.1007/s00710-024-00878-x.

Acknowledgements This work was supported by the Charles University Grant Agency, (GAUK 502120, to MJ), and by the Grant Agency of Czech Republic (GA ČR 23–04734 S, to VŠ). Many thanks to reviewer Alexandr S. Stepanov, editor-in-chief Lutz Nasdala, and an anonymous expert for their constructive reviews, and also to journal editor Chao Wang for helpful comments during the review process.

Funding Open access publishing supported by the National Technical Library in Prague.

References

Aigner-Torres M, Blundy J, Ulmer P, Pettke T (2007) Laser ablation ICPMS study of trace element partitioning between plagioclase and basaltic melts: an experimental approach. Contrib Mineral Petrol 153:647–667. https://doi.org/10.1007/s00410-006-0168-2

Anand M, Tartèse R, Barnes JJ (2014) Understanding the origin and evolution of water in the Moon through lunar sample studies. Philosophical Trans Royal Soc A: Math Phys Eng Sci 372. https://doi.org/10.1098/rsta.2013.0254

Anders E, Grevesse N (1989) Abundances of the elements: meteoritic and solar. Geochim Cosmochim Acta 53:197–214. https://doi.org/10.1016/0016-7037(89)90286-X

Arzamastsev AA, Arzamastseva LV, Bea F, Montero P (2009) Trace elements in minerals as indicators of the evolution of alkaline ultrabasic dike series: LA-ICP-MS data for the magmatic provinces of northeastern Fennoscandia and Germany. Petrology 17:46–72. https://doi.org/10.1134/S0869591109010032

Blundy J, Wood B (1994) Prediction of crystal–melt partition coefficients from elastic moduli. Nature 372:452–454. https://doi.org/10.1038/372452a0

Blundy J, Wood B (2003) Mineral-melt partitioning of uranium, thorium and their daughters. Rev Mineral Geochem 52:59–123. https://doi.org/10.2113/0520059

Blundy JD, Robinson JAC, Wood BJ (1998) Heavy REE are compatible in clinopyroxene on the spinel lherzolite solidus. Earth Planet Sci Lett 160:493–504. https://doi.org/10.1016/S0012-821X(98)00106-X

Borisov SV, Klevtsova RF (1963) The crystal structure of REE-Sr apatite. Zh Struct Khim 4:629–631

Boyce JW, Tomlinson SM, McCubbin FM, Greenwood JP, Treiman AH (2014) The lunar apatite paradox. Science 344:400–402. https://doi.org/10.1126/science.1250398

Brophy JG, Ota T, Kunihro T, Tsujimori T, Nakamura E (2011) In situ ion-microprobe determination of trace element partition coefficients for hornblende, plagioclase, orthopyroxene, and apatite in equilibrium with natural rhyolitic glass, little Glass Mountain Rhyolite, California. Am Mineral 96:1838–1850. https://doi.org/10.2138/am.2011.3857

Bruand E, Fowler M, Storey C, Darling J (2017) Apatite trace element and isotope applications to petrogenesis and provenance. Am Mineral 102:75–84. https://doi.org/10.2138/am-2017-5744

Chen J, Jolliff BL, Wang A et al (2019) Petrogenesis and shock metamorphism of basaltic lunar meteorites Northwest Africa 4734 and 10597. J Geophys Res: Planet 124:2583–2598. https://doi.org/10.1029/2019JE006084

Cockbain AG, Smith GV (1967) Alkaline-earth-rare-earth silicate and germanate apatites. Mineral Mag J M Soc 36:411–421. https://doi.org/10.1180/minmag.1967.036.279.11

Dong ZL, White TJ (2004a) Calcium–lead fluoro-vanadinite apatites. I. Disequilibrium structures. Acta Crystallogr B 60:138–145. https://doi.org/10.1107/S0108768104001831

Dong ZL, White TJ (2004b) Calcium–lead fluoro-vanadinite apatites. II. Equilibrium structures. Acta Crystallogr B 60:146–154. https://doi.org/10.1107/S0108768104001843

Dygert N, Liang Y, Sun C, Hess P (2014) An experimental study of trace element partitioning between Augite and Fe-rich basalts. Geochim Cosmochim Acta 132:170–186. https://doi.org/10.1016/j.gca.2014.01.042

Elliott JC, Wilson RM, Dowker SEP (2002) Apatite structures. Adv X Ray Anal 45:172–181

Fabbrizio A, Schmidt MW, Petrelli M (2021) Effect of fO2 on Eu partitioning between clinopyroxene, orthopyroxene and basaltic melt: development of a Eu3+/Eu2+oxybarometer. Chem Geol 559:119967. https://doi.org/10.1016/j.chemgeo.2020.119967

Fedele L, Lustrino M, Melluso L, Morra V, Zanetti A, Vannucci R (2015) Trace-element partitioning between plagioclase, alkali feldspar, Ti-magnetite, biotite, apatite, and evolved potassic liquids from Campi Flegrei (Southern Italy). Am Mineral 100:233–249. https://doi.org/10.2138/am-2015-4995

Fleet ME, Pan Y (1995) Site preference of rare earth elements in fluorapatite. Am Mineral 80:329–335. https://doi.org/10.2138/am-1995-3-414

Fleet ME, Pan Y (1997) Site preference of rare earth elements in fluorapatite: Binary (LREE+HREE)-substituted crystals. Am Mineral 82:870–877. https://doi.org/10.2138/am-1997-9-1004

Fleet ME, Liu X, Pan Y (2000a) Rare-earth elements in chlorapatite [Ca10 (PO4) 6Cl2]: Uptake, site preference, and degradation of monoclinic structure. Am Mineral 85:1437–1446. https://doi.org/10.2138/am-2000-1012

Fleet ME, Liu X, Pan Y (2000b) Site preference of rare earth elements in hydroxyapatite [Ca10 (PO4) 6 (OH) 2]. J Solid State Chem 149:391–398. https://doi.org/10.1006/jssc.1999.8563

Fujimaki H (1986) Partition coefficients of Hf, Zr, and REE between zircon, apatite, and liquid. Contrib Mineral Petrol 94:42–45

Gaetani GA, Kent AJ, Grove TL, Hutcheon ID, Stolper EM (2003) Mineral/melt partitioning of trace elements during hydrous peridotite partial melting. Contrib Mineral Petrol 145:391–405. https://doi.org/10.1007/s00410-003-0447-0

Harms E, Gardner JE, Schmincke HU (2004) Phase equilibria of the Lower Laacher see Tephra (East Eifel, Germany): constraints on pre-eruptive storage conditions of a phonolitic magma reservoir. J Volcanol Geoth Res 134:125–138. https://doi.org/10.1016/j.jvolgeores.2004.01.009

Harrison TM, Watson EB (1984) The behavior of apatite during crustal anatexis: equilibrium and kinetic considerations. Geochim Cosmochim Acta 48:1467–1477. https://doi.org/10.1016/0016-7037(84)90403-4

Hauri EH, Wagner TP, Grove TL (1994) Experimental and natural partitioning of Th, U, Pb and other trace elements between garnet, clinopyroxene and basaltic melts. Chem Geol 117:149–166. https://doi.org/10.1016/0009-2541(94)90126-0

Hiesinger H, Jaumann R, Neukum G, Head JW III (2000) Ages of mare basalts on the lunar nearside. J Geophys Res: Planet 105:29239–29275. https://doi.org/10.1029/2000JE001244

Hiesinger H, Head JW III, Wolf U, Jaumann R, Neukum G (2003) Ages and stratigraphy of mare basalts in oceanus procellarum, mare nubium, mare cognitum, and mare insularum. J Geophys Res: Planet 108. https://doi.org/10.1029/2002JE001985

Hoskin PW, Kinny PD, Wyborn D, Chappell BW (2000) Identifying accessory mineral saturation during differentiation in granitoid magmas: an integrated approach. J Petrol 41:1365–1396. https://doi.org/10.1093/petrology/41.9.1365

Hughes JM, Cameron M, Crowley KD (1989) Structural variations in natural F, OH, and cl apatites. Am Mineral 74:870–876

Hughes JM, Cameron M, Mariano AN (1991) Rare-earth-element ordering and structural variations in natural rare-earth-bearing apatites. Am Mineral 76:1165–1173

Ji D, Dygert N (2024) Trace element partitioning between apatite and silicate melts: effects of major element composition, temperature, and oxygen fugacity, and implications for the volatile element budget of the lunar magma ocean. Geochim Cosmochim Acta 369:141–159. https://doi.org/10.1016/j.gca.2023.11.004

Jiang Y, Kang J, Liao S, Elardo SM et al (2023) Fe and mg isotope compositions indicate a hybrid mantle source for young Chang'E 5 mare basalts. Astrophys J Lett 945:L26. https://doi.org/10.3847/2041-8213/acbd31

Jonsson E, Harlov DE, Majka J, Högdahl K, Persson-Nilsson K (2016) Fluorapatite-monazite-allanite relations in the Grängesberg apatite-iron oxide ore district, Bergslagen, Sweden. Am Mineral 101:1769–1782. https://doi.org/10.2138/am-2016-5655

Klemme S, Dalpé C (2003) Trace-element partitioning between apatite and carbonatite melt. Am Mineral 88:639–646. https://doi.org/10.2138/am-2003-0417

Kovalenko VI, Antipin VS, Vladykin NV, Smirnova EV, Balashov YA (1982) REE partition ratios in apatites and REE behavior in magmatic processes. Geokhimiya 2:230–243

Lee CTA, Harbert A, Leeman WP (2007) Extension of lattice strain theory to mineral/mineral rare-earth element partitioning: an approach for assessing disequilibrium and developing internally consistent partition coefficients between olivine, orthopyroxene, clinopyroxene and basaltic melt. Geochim Cosmochim Acta 71:481–496. https://doi.org/10.1016/j.gca.2006.09.014

Li W, Costa F (2020) A thermodynamic model for F-Cl-OH partitioning between silicate melts and apatite including non-ideal mixing with application to constraining melt volatile budgets. Geochim Cosmochim Acta 269:203–222. https://doi.org/10.1016/j.gca.2019.10.035

Li H, Hermann J (2017) The effect of fluorine and chlorine on trace element partitioning between apatite and sediment melt at subduction zone conditions. Chem Geol 473:55–73. https://doi.org/10.1016/j.chemgeo.2017.10.016

Li W, Costa F, Oppenheimer C, Nagashima K (2023) Volatile and trace element partitioning between apatite and alkaline melts. Contrib Mineral Petrol 178:9. https://doi.org/10.1007/s00410-022-01985-8

Mackie PE, Young RA (1973) Location of nd dopant in fluorapatite, Ca5 (PO4) 3F: nd. J Appl Crystallogr 6:26–31. https://doi.org/10.1107/S0021889873008009

Mahood GA, Stimac JA (1990) Trace-element partitioning in pantellerites and trachytes. Geochim Cosmochim Acta 54:2257–2276. https://doi.org/10.1016/0016-7037(90)90050-U

McCubbin FM, Ustunisik G (2018) Experimental investigation of F and cl partitioning between Apatite and Fe-rich basaltic melt at 0 GPa and 950–1050 C: evidence for steric controls on apatite-melt exchange equilibria in OH-poor apatite. Am Mineral 103:1455–1467. https://doi.org/10.2138/am-2018-6339

McDade P, Blundy JD, Wood BJ (2003) Trace element partitioning on the Tinaquillo Lherzolite solidus at 1.5 GPa. Phys Earth Planet in 139:129–147. https://doi.org/10.1016/S0031-9201(03)00149-3

Mercier PH, Le Page Y, Whitfield PS, Mitchell LD, Davidson IJ, White TJ (2005) Geometrical parameterization of the crystal chemistry of P63/m apatites: comparison with experimental data and ab initio results. Acta Crystallogr B 61:635–655. https://doi.org/10.1107/S0108768105031125

Nagasawa H (1970) Rare earth concentrations in zircons and apatites and their host dacites and granites. Earth Planet Sci Lett 9:359–364. https://doi.org/10.1016/0012-821X(70)90136-6

Nagasawa H, Schnetzler CC (1971) Partitioning of rare earth, alkali and alkaline earth elements between phenocrysts and acidic igneous magma. Geochim Cosmochim Acta 35:953–968. https://doi.org/10.1016/0016-7037(71)90008-1

Nathwani CL, Loader MA, Wilkinson JJ, Buret Y, Sievwright RH, Hollings P (2020) Multi-stage arc magma evolution recorded by apatite in volcanic rocks. Geology 48:323–327. https://doi.org/10.1130/G46998.1

O'Neill HSC, Eggins SM (2002) The effect of melt composition on trace element partitioning: an experimental investigation of the activity coefficients of FeO, NiO, CoO, MoO2 and MoO3 in silicate melts. Chem Geol 186:151–181. https://doi.org/10.1016/S0009-2541(01)00414-4

Onuma N, Higuchi H, Wakita H, Nagasawa H (1968) Trace element partition between two pyroxenes and the host lava. Earth Planet Sci Lett 5:47–51. https://doi.org/10.1016/S0012-821X(68)80010-X

Padilla AJ, Gualda GA (2016) Crystal-melt elemental partitioning in silicic magmatic systems: an example from the Peach Spring Tuff high-silica rhyolite, Southwest USA. Chem Geol 440:326–344. https://doi.org/10.1016/j.chemgeo.2016.07.004

Parat F, Holtz F (2005) Sulfur partition coefficient between apatite and rhyolite: the role of bulk S content. Contrib Mineral Petrol 150:643–651. https://doi.org/10.1007/s00410-005-0041-8

Pelullo C, Iovine RS, Arienzo I, Di Renzo V, Pappalardo L, Petrosino P, D'Antonio M (2022) Mineral-melt equilibria and geothermobarometry of Campi Flegrei magmas: inferences for magma storage conditions. Mineral-Basel 12:308. https://doi.org/10.3390/min12030308

Prowatke S, Klemme S (2006) Trace element partitioning between apatite and silicate melts. Geochim Cosmochim Acta 70:4513–4527. https://doi.org/10.1016/j.gca.2006.06.162

R Core Team (2021) R: a Language and Environment for Statistical Computing. R Foundation for Statistical Computing, Vienna. https://www.R-project.org

Rapp JF, Draper DS (2018) Fractional crystallization of the lunar magma ocean: updating the dominant paradigm. Meteorit Planet Sci 53:1432–1455. https://doi.org/10.1111/maps.13086

Ryerson FJ, Hess PC (1978) Implications of liquid-liquid distribution coefficients to mineral-liquid partitioning. Geochim Cosmochim Acta 42:921–932. https://doi.org/10.1016/0016-7037(78)90103-5

Sano Y, Terada K, Fukuoka T (2002) High mass resolution ion microprobe analysis of rare earth elements in silicate glass, apatite and zircon: lack of matrix dependency. Chem Geol 184:217–230. https://doi.org/10.1016/S0009-2541(01)00366-7

Schoneveld L, O'Neill HSC (2019) The influence of melt composition on the partitioning of trace elements between anorthite and silicate melt. Contrib Mineral Petrol 174:1–18. https://doi.org/10.1007/s00410-019-1548-8

Shannon RD (1976) Revised effective ionic radii and systematic studies of interatomic distances in halides and chalcogenides. Acta Crystallogr A 32:751–767. https://doi.org/10.1107/S0567739476001551

Shearer CK, Papike JJ (1999) Magmatic evolution of the Moon. Am Mineral 84:1469–1494. https://doi.org/10.2138/am-1999-1001

Shimizu K, Liang Y, Sun C, Jackson CR, Saal AE (2017) Parameterized lattice strain models for REE partitioning between amphibole and silicate melt. Am Mineral 102:2254–2267. https://doi.org/10.2138/am-2017-6110

Stadermann AC, Zanetti MR, Jolliff BL, Hiesinger H, van der Bogert CH, Hamilton CW (2018) The age of lunar mare basalts south of the Aristarchus Plateau and effects of secondary craters formed by the Aristarchus event. Icarus 309:45–60. https://doi.org/10.1016/j.icarus.2018.02.030

Stepanov AS, Zhukova IA, Jiang SY (2023) Experimental constraints on miscibility gap between apatite and britholite and REE partitioning in an alkaline melt. Am Mineral 108:1043–1052. https://doi.org/10.2138/am-2022-8535

Sun C, Liang Y (2012) Distribution of REE between clinopyroxene and basaltic melt along a mantle adiabat: effects of major element composition, water, and temperature. Contrib Mineral Petrol 163:807–823. https://doi.org/10.1007/s00410-011-0700-x

Sun C, Liang Y (2013a) The importance of crystal chemistry on REE partitioning between mantle minerals (garnet, clinopyroxene, orthopyroxene, and olivine) and basaltic melts. Chem Geol 358:23–36. https://doi.org/10.1016/j.chemgeo.2013.08.045

Sun C, Liang Y (2013b) Distribution of REE and HFSE between low-Ca pyroxene and lunar picritic melts around multiple saturation points. Geochim Cosmochim Acta 119:340–358. https://doi.org/10.1016/j.gca.2013.05.036

Sun C, Graff M, Liang Y (2017) Trace element partitioning between plagioclase and silicate melt: the importance of temperature and plagioclase composition, with implications for terrestrial and lunar magmatism. Geochim Cosmochim Acta 206:273–295. https://doi.org/10.1016/j.gca.2017.03.003

Tailby ND, Trail D, Watson B, Lanzirotti A, Newville M, Wang Y (2023) Eu speciation in apatite at 1 bar: an experimental study of valence-state partitioning by XANES, lattice strain, and Eu/Eu* in basaltic systems. Am Mineral: J Earth Planet Mater 108:789–813. https://doi.org/10.2138/am-2022-8388

Urusov VS, Khudolozhkin VO (1974) Energy analysis of cation ordering in the structure of apatite. Geochem Int—11:1048–1053

Venezky DY, Rutherford MJ (1999) Petrology and Fe–Ti oxide reequilibration of the 1991 Mount Unzen mixed magma. J Volcanol Geoth Res 89:213–230. https://doi.org/10.1016/S0377-0273(98)00133-4

Watson EB (1976) Two-liquid partition coefficients: experimental data and geochemical implications. Contrib Mineral Petrol 56:119–134

Watson EB, Green TH (1981) Apatite/liquid partition coefficients for the rare earth elements and strontium. Earth Planet Sci Lett 56:405–421. https://doi.org/10.1016/0012-821X(81)90144-8

Watson EB, Harrison TM (1984) Accessory minerals and the geochemical evolution of crustal magmatic systems: a summary and prospectus of experimental approaches. Phys Earth Planet in 35:19–30. https://doi.org/10.1016/0031-9201(84)90031-1

Webster JD, Piccoli PM (2015) Magmatic apatite: a powerful, yet deceptive, mineral. Elements 11:177–182. https://doi.org/10.2113/gselements.11.3.177

White JC (2003) Trace-element partitioning between alkali feldspar and peralkalic quartz trachyte to rhyolite magma. Part II: empirical equations for calculating trace-element partition coefficients of large-ion lithophile, high field-strength, and rare-earth elements. Am Mineral 88:330–337. https://doi.org/10.2138/am-2003-2-310

White TJ, Dong Z (2003) Structural derivation and crystal chemistry of apatites. Acta Crystallogr B 59:1–16. https://doi.org/10.1107/S0108768102019894

White JC, Holt GS, Parker DF, Ren M (2003) Trace-element partitioning between alkali feldspar and peralkalic quartz trachyte to rhyolite magma. Part I: systematics of trace-element partitioning. Am Mineral 88:316–329. https://doi.org/10.2138/am-2003-2-309

White JC, Parker DF, Ren M (2009) The origin of trachyte and pantellerite from Pantelleria, Italy: insights from major element, trace element, and thermodynamic modelling. J Volcanol Geoth Res 179:33–55. https://doi.org/10.1016/j.jvolgeores.2008.10.007

Wood BJ, Blundy JD (1997) A predictive model for rare earth element partitioning between clinopyroxene and anhydrous silicate melt. Contrib Mineral Petrol 129:166–181

Wörrier G, Beusen JM, Duchateau N, Gijbels R, Schmincke HU (1983) Trace element abundances and mineral/melt distribution coefficients in phonolites from the Laacher See Volcano (Germany). Contrib Mineral Petrol 84:152–173

Wu Y, Hsu W (2020) Mineral chemistry and in situ UPb geochronology of the mare basalt Northwest Africa 10597: implications for low-Ti mare volcanism around 3.0 Ga. Icarus 338:113531. https://doi.org/10.1016/j.icarus.2019.113531

Yao L, Sun C, Liang Y (2012) A parameterized model for REE distribution between low-Ca pyroxene and basaltic melts with applications to REE partitioning in low-Ca pyroxene along a mantle adiabat and during pyroxenite-derived melt and peridotite interaction. Contrib Mineral Petrol 164:261–280. https://doi.org/10.1007/s00410-012-0737-5